TRI-PP-90-62
Aug 1990

MULTI-NUCLEON PION ABSORPTION IN THE ^{4}He(π^+,ppp)n REACTION

P. Weber*, J. McAlister, R. Olszewski, A. Feltham, M. Hanna, R.R. Johnson, M. Pavan, C. Ponting, F.M. Rozon, M. Sevior, V. Sossi, D. Vetterli
University of British Columbia, Vancouver, B.C. V6T 2A6, Canada
and
D. Humphrey†, G.J. Lolos, Z. Papandreou
University of Regina, Regina, SK, S4S 0A2, Canada
and
R. Tacik‡
University of Karlsruhe, 7500 Karlsruhe, Federal Republic of Germany
and
D. Ottewell, G. Sheffer, G.R. Smith
TRIUMF, 4004 Wesbrook Mall, Vancouver, B.C. V6T 2A3, Canada
and
Y. Mardor, S. May-Tal
Raymond and Beverly Sackler Faculty of Exact Sciences,
Department of Physics, Tel-Aviv University, Ramat Aviv, Israel 69978

Abstract

Three-proton emission cross sections for the ^{4}He(π^+, ppp)n reaction were measured at an incident pion kinetic energy of $T_{\pi+}$=165 MeV over a wide angular range in a kinematically complete experiment. Angular correlations, missing momentum distributions and energy spectra are compared with three- and four-body phase space Monte Carlo calculations. The results provide strong evidence that most of the three-proton coincidences result from three-nucleon absorption. From phase-space integration the total three-nucleon absorption cross section is estimated to be σ^{3N} = 4.8 ± 1.0 mb. The cross section involving four nucleons is small and is estimated to be $\sigma^{4N} < 2$ mb. On the scale of the total absorption cross section in ^{4}He, multi-nucleon pion absorption seems to represent only a small fraction.

PACS: 25.80

(to be submitted to Physical Review C)

*present affiliation: IMP/ETH Zürich, mailing address: EP-Div CERN, 1211 Geneve 23, Switzerland
†permanent address: Western Kentucky University, Bowling Green, KY 42101, USA
‡permanent address: Physics department, University of Regina, Regina, SK, S4S 0A2, Canada

1. INTRODUCTION

Pion absorption studies in the past were focused predominantly on the fundamental reaction $\pi d \rightarrow pp$ and its associated reaction in nuclei $\pi NN \rightarrow NN$ from threshold across the Δ resonance, establishing the picture of 2N absorption (2NA) with the prominent signature of two nucleons emitted with high kinetic energy and correlated angles[1]. Recent experiments regarding pion absorption mechanisms involving more than two nucleons have attracted considerable interest. The experimental observations supporting the existence of absorption mechanisms beyond the 2NA model, either directly or indirectly, come from comparisons of two-nucleon absorption cross sections with total absorption cross sections, from triple-coincidence experiments, or from nucleon-nucleon coincidences where either the kinematics or charge conservation excludes a direct 2NA process.

Pions in nuclei are preferentially absorbed on pn pairs with the same quantum number, $^3S_1$(T=0), as the free deuteron. The energy dependence of the 2N cross section reflects the presence of a Δ in the intermediate state, and thus pion absorption on two nucleons is commonly described in terms of $\pi NN \rightarrow \Delta N \rightarrow NN$. At first glance, 2NA in nuclei resembles the free process[1] and therefore it is often referred to as quasifree two-nucleon absorption (QFA). However, the QFA reaction is disturbed by the nuclear medium, i.e. binding energy, Fermi motion, excitation of the residual nucleus, Pauli exclusion principle, and secondary processes such as initial state interactions of pions with nucleons (ISI) as well as final state interactions of emerging nucleons with the rest of the nucleus (FSI). These nuclear medium effects render quantitative comparisons more difficult, which applies particularly to the question of how much of the total absorption cross section is due to 2NA.

For carbon the 2NA cross section $d\sigma/d\Omega(^{12}C(\pi^+, pp)X)$ was isolated from the angular correlation $d^2\sigma(\theta_2)/d\Omega_1 d\Omega_2$ and integrated over the full space at T_{π^+}=165 and 245 MeV[2]. From the comparison with total absorption cross sections it was concluded that only $\sim$ 10% of the total absorption cross section is due to 2NA. Even if final state interactions (FSI) of the outgoing nucleons with the rest of the nucleus were accounted for, a substantial fraction of the total absorption cross section remains unexplained. This experimental observation suggests indirectly the existence of absorption mechanisms beyond the 2NA model, which are necessary to explain the "missing cross section". For heavier nuclei like ^{16,18}O, Fe, and Bi the ratio of σ^{2N}/σ_{tot} was found to be even smaller than 10 %[3]. The differential cross sections $d\sigma^{2N}/d\Omega$ were obtained by fitting a narrow Gaussian to the part of the data which is - apart from Fermi motion - consistent with the $\pi d \rightarrow pp$ reaction, and by subtracting a broad Gaussian underneath the narrow one attributed to ISI, FSI, and more complicated pion absorption mechanisms. Similar measurements were performed with ^{58}Ni[4], where the data were analyzed with various cuts on the sum of proton kinetic energies. The conclusion was that in any case less than 50 % of the absorption cross section arises from absorption on nucleon pairs. This two-Gaussian method of deducing 2N cross sections was criticized by Ritchie et al.[5]. Their calculation of two-nucleon absorption in the distorted-wave impulse approximation (DWIA) showed that the quasi-deuteron component of the $^{12}C(\pi^+, pp)$ reaction[3] could have substantial broad components in the two-nucleon angular correlation because of the different shape of angular correlations for L=0 and L=2, the relative angular momentum of the two absorbing nucleons with respect to the residual nucleus. An intranuclear cascade calculation (INC) by Gibbs

and Kaufmann[6] based on the ^{58}Ni data resulted in as much as 70 % two-nucleon absorption.

A measurement on $^{16}O(\pi^+,pp)$[7] with good excitation energy resolution clarified the experimental situation to some extent, as specific final states with defined angular momentum could be isolated. Their angular correlation demonstrated the dependence on the angular momentum transfer (L > 0 contributions lead to wider angular correlations) which makes the two-Gaussian decomposition method unreliable. The result is that $\sim$ 20% of the π^+ absorption cross section on ^{16}O at T_π=116 MeV leads to the emission of two protons and low excitation energy of the residual nucleus system (E_x < 20 MeV). Substantial 2NA strength was also observed for higher excitation energy. The inclusion of corrections for FSI results in > 50% 2NA which makes it the dominant process. However, it should be noted that data were extrapolated into unmeasured regions of phase space and corrections for FSI are large. Also the conclusion of additional 2NA strength at high excitation energy is uncertain to some extent because the angular correlation of multi-nucleon final states peaks at the same angle. A similar experiment[8] was carried out with solid state detectors at T_π=59.4 MeV on ^{6,7}Li. Multiple-differential cross sections for individual states of the residual nucleus were extracted and compared with the $\pi d \rightarrow pp$ reaction. The main result is that pion absorption on a pn pair leading to the helium ground state, $\sigma(^6Li(\pi^+,pp)^4He(g.s.))$ = 6.7 mb, is the same as for the $\pi d \rightarrow pp$ reaction. This was not so surprising because the quasi-deuteron cluster (p-shell nucleons), which is removed from the nucleus, is only bound by 1.47 MeV. However, about twice the $\pi d \rightarrow pp$ strength was found at higher excitation energy, i.e. $\sigma(^6Li(\pi^+,pp)^4He(E_x = 20 - 35MeV))$ = 13.7 mb. Consequently the total 2NA strength is 20 mb, which is $\sim$ 60% of the total absorption cross section (36$\pm$10 mb). At T_π=160 MeV, however, the 2NA strength could drop to only 30%[8], because the total absorption cross section is increasing much faster with pion energy than the $\pi d \rightarrow pp$ cross section. No corrections for FSI were applied to the Li data, in contrast to Ref.[7].

It is clear that the 2NA strength can be extracted much more accurately in experiments with good excitation energy resolution[7,8] than from the angular correlation measurements[2,3]. The extrapolations into unmeasured regions, corrections for FSI, and the rather semantic question of whether pion absorption leading to high excitation (above particle emission stability) of the residual nucleus can be counted as 2NA or has to be considered as a pion absorption mode with multi-particle emission, pose the question whether a firm number can be placed for the fraction of 2NA.

Less model-dependent is the situation in ^{3}He, where the quasi-deuteron absorption can be studied in the absence of shell effects, and the secondary processes like ISI and FSI can be assumed to be rather minor. Extensive pion absorption investigations were carried out on nucleon pairs with quantum numbers T=0, S=1 and T=1, S=0 in the reactions $^3He(\pi^+,pp)p$ and $^3He(\pi^-,pn)n$. The cross section for the latter reaction was found to be smaller by an order of magnitude compared to the former[9-13], because p-wave absorption cannot proceed via a $^5S_2$ ΔN intermediate state. The former reaction scales with the number of nucleon pairs, i.e. $\sigma(^3He(\pi^+,pp)p) \sim 1.5\times\sigma(^2H(\pi^+,pp))$. In addition to these measurements with counter configurations at conjugate angles (according to the $\pi d \rightarrow pn$ kinematics), configurations with the detectors at off-conjugate angles scanned the three-nucleon phase space far away from the two-body reaction. Surprisingly, the two-fold differential cross section $d^2\sigma/d\Omega_1 d\Omega_2$ did not vanish even

at angles 80 to 100 degrees off the conjugate angle. The comparison of these events with a three-nucleon (3N) phase space calculation resulted in a strong correlation between the cross section and the 3N phase space with an almost constant matrix element[14]. This mechanism is referred to as three-nucleon absorption (3NA). The ratio of σ^{3N}/σ^{2N} was determined to be $\sim (20-40)\%$ for pion energies below the Δ-resonance[12,14]. This three-nucleon absorption cross section was believed to explain a part of the "missing cross section". Data on ^{3}He(π^+, pp)p are now also available above the resonance ($T_\pi = 350, 500$ MeV)[15] with $\sigma(^3\mathrm{He}(\pi^+, \mathrm{pp})\mathrm{p}) > 1.5\times\sigma(^2\mathrm{H}(\pi^+, \mathrm{pp}))$ and the three-nucleon absorption cross section σ^{3N} being $\sim 45\%$ of the total absorption cross section.

Evidence for 3NA in larger nuclei came from experiments detecting three protons in coincidence. The first three-proton coincidences were reported from the reaction ^{12}C(π^+, ppp)X. One experiment[16] searched for two-step processes, where a pion is first back-scattered in a $\pi N \rightarrow \pi' N$ reaction (ISI) and then subsequently absorbed by two nucleons leading to a high-energy nucleon in backward direction. No evidence was found for a two-step process but a large number of three-proton events was observed. No conclusive reaction mechanism was suggested to explain the data. The experiment of Ref.[16] was subsequently repeated with larger phase space coverage, at two additional energies[17]. Data were compared with Monte Carlo (MC) phase space calculations simulating three- and four-nucleon absorption. On the basis of such comparisons with the angular correlations between the detected protons and their momentum distributions, it was concluded that the absorption process giving rise to the majority of the observed events, involved three nucleons and not four or more. The measured proton energy distributions were not well described by the phase space calculations unless nuclear excitation was taken into account. Estimates were made for the total three-nucleon absorption cross sections (8 mb, 20 mb, and 22 mb at $T_\pi = 130$, 180, and 228 MeV). Although these values are larger than σ^{3N}_{ppp} measured for ^{3}He, they represent smaller fractions of the total absorption cross section, i.e. 5, 11, and 19% respectively, and thus cannot account for the "missing cross section".

The experiment of Ref.[18] searched for a narrow structure in the energy spectrum of forward going protons from the ^{12}C(π^+, ppp)X reaction as a signature of a bound Δ in the nucleus. No narrow structure (less than 20 MeV) was found but a broad structure, superimposed on a continuum background, was observed for three different pion momenta. The broad structure was interpreted as quasifree scattering of the pion before capture. Cross sections to various final states were estimated, in partial agreement with an early bubble chamber experiment[19], which found that $\sim 79\%$ of the absorptions produced three or more nucleons or had more than 60 MeV missing. Only 9.5 % of the total absorption cross section was due to quasi-deuteron absorption with little missing energy, which is in agreement with Ref.[2], and $\sim 40\%$ came from absorption on an α cluster. In a large fraction of the events neutrals were released too.

The (π^-, pp) reaction provides further information on the existence of non-2N absorption mechanisms. It is obvious by charge conservation that three nucleons must be involved in this reaction, either in a two-step process ISI+2N or 2N+FSI, or in a direct reaction π^-ppp $\rightarrow$ ppn. Angular correlation studies on ^{6}Li and ^{12}C[20] compared to INC calculations favour multiple-scattering processes. The ^{12}C(π^-, pp) experiment was repeated by Papandreou et al.[21] with the result that the double peak

observed by Ref.[20] was not reproduced but an enhancement of events over three-body phase space showed up in between the two peaks.

As a next-step, ^{4}He is an ideal nucleus for pion absorption studies beyond the 2NA model for various reasons:
1) The reaction ^{4}He(π, NNN)N can be studied in kinematically complete manner when performing a triple coincidence experiment.
2) The presence of four nucleons offers more reaction channels than in ^{3}He and therefore allows a more general exploration of multi-nucleon emission following pion absorption.
3) The nuclear medium effects are still minimized and the ^{4}He wave-function is well known.

Recently 3NA cross sections were measured in the reactions ^{4}He(π^+, ppp)n and ^{4}He(π^+, ppn)p in a kinematically complete experiment[22] for one angle setting at T_{π^+}=120 MeV. The momentum distribution of the unobserved nucleon was compared with MC calculations, which demonstrated the prevalence of 3NA over 4NA. The cross sections for ppp- and ppn- emission were integrated and are comparable to σ^{3N} in ^{3}He. Interestingly, σ^{3N}_{ppn} exceeds σ^{3N}_{ppp} by a factor of two.

In the present work we investigated the reaction ^{4}He(π^+, ppp)n at T_{π^+}=165 MeV over a wide angular range in a kinematically complete experiment. The momentum distribution of the unobserved neutron is one observable that characterizes the reaction. Another important observable which enables one to draw conclusions about the reaction mechanism is the angular correlation of the protons. This observable can be explored by fixing the angle of two protons and measuring the angular distribution of the third proton; three different settings were chosen. Studying the angular distribution of the protons in such a systematic way adds to the confidence when differential cross sections are integrated, rather than inferring the cross section from a small solid angle. The present experiment covers a solid angle of $\Delta\Omega \sim 0.8sr$, with only out-of-plane measurements and proton detection along the beam axis excluded.

2. EXPERIMENT

The experiment was carried out at the TRIUMF M11 medium energy pion channel. The experimental set-up is depicted in Fig. 1. Pions of 165 MeV incident kinetic energy, which were monitored by a scintillator hodoscope (Hodo) and a thin scintillation counter (S1), impinged upon a liquid ^{4}He target of 1.07 ± 0.03 g/cm^2 areal density. Protons from the reaction ^{4}He(π^+, ppp)n were detected in any triple coincidence between the total absorption counters RA and RB ("Regina" counters) and the time-of-flight (TOF) counters TA and TB ("Tel Aviv" bars). Each detector was equipped with a thin ΔE counter for particle identification and charged particle trigger, and Multi Wire Proportional Chambers (MWPC) were used to determine trajectories and to trace the events back to the target.

Several counter settings were chosen with the objective of favouring either the three-nucleon or four-nucleon phase space, in order to obtain the sensitivity which is necessary to distinguish between different reaction mechanisms. For each setting one of the counters (RB) was displaced by $+15^0$ and -15^0 from a nominal position, keeping all the other detectors at the same angle. This angle variation increases the sensitivity to a three-nucleon process, because the selection of three angles and the energy thresholds of the detectors constrain the 3N phase space considerably more than

the 4N phase space. The angular distribution of the protons was measured with the segmented counters TA and TB for each angle setting of RA and RB. A compilation of all the counter configurations is given in Table 1 (23 possible combinations).

During calibration runs a liquid D_2 target and a solid CD_2 target were employed for calibrating the energy response of the Regina counters and the TOF of the Tel Aviv bars via the $\pi^+ d \rightarrow pp$ and the $\pi^+ p \rightarrow \pi^+ p$ reactions. Two incident pion energies, $T_\pi = 65$ and 165 MeV, and numerous counter combinations of RA · RB, RA · TB and RB · TA at kinematically correct angles were chosen to allow for as wide a range of calibration energies as possible. The $\pi^+ d \rightarrow pp$ reaction also served as a benchmark in order to check the beam normalization and to determine the reaction losses and edge effects of stopping protons in RA and RB.

The hardware trigger required a double or a triple coincidence. A multiplicity logic unit (MLU) selected the events according to the desired level. During data taking the coincidence level was set to three for most of the runs, i.e. MLU=3, and events from any three out of four detectors were recorded on tape. Some runs were duplicated with MLU=2 allowing for a consistency check, accepting any two-fold and three-fold coincidences. In this case the two-fold coincidences were prescaled appropriately (up to 64) to accumulate a comparable amount of each event type and to keep the dead time of the data acquisition to a minimum, which allowed the majority of all triple-coincidences to be recorded on tape. The three-fold coincidence was subsequently demanded in the software off-line analysis. All the calibration runs were taken with MLU=2.

2.1 The Liquid ^{4}He Target

A schematic diagram of the cryogenic ^{4}He target is given in Fig. 2. The target flask is a vertical cylinder of 7.62 cm diameter and is made of a thin 0.125 mm mylar foil. All other windows intercepted by the pions were also very thin in order to keep the background low and to minimize the ionization losses for low-energy charged particles. Two aluminum foils served for temperature insulation and the two outermost windows (made of mylar and kapton, respectively) contained the vessel vacuum. The liquid ^{4}He was kept at 1.5 ± 0.1 K corresponding to a density of 0.145 g/cm^3, equivalent to $2.18 \cdot 10^{22}$ ^{4}He nuclei /cm^3. Slight variations of the temperature did not affect the density (normalization), because the density of liquid ^{4}He is constant at < 1.8K. The effective thickness of the target was corrected for the size of the beam spot and for the length contraction of mylar at 1.5 K. The length contraction accounts for $\sim (1 - 1.5)\%$ reduction in diameter. The beam distribution of 2 cm width was folded in with the shape of the target cell, which reduces the thickness of the target by another 2%. The effective target thickness is 7.4±0.2cm.

The liquid ^{2}H target was similar in construction. The diameter of the target cell was 5.08 cm, which corresponds to an effective target thickness of 4.88 cm at 23 K.

2.2 The Regina Counters, RA and RB

These detectors were described in detail elsewhere[23], however, a brief description will be given here.

The Regina counters consist of two arm-assemblies labelled RA and RB each of which is further divided into two sub-assemblies labelled 'right' and 'left'. The front

area of each sub-assembly is $20 \times 10\,cm^2$ leading to a total of $20 \times 20\,cm^2$ for each arm. The arms employ a $\Delta E - E$ counter arrangement, with all detectors constructed out of BC400 plastic scintillator material and placed at $\approx$ 46 cm from the target. The ΔE counters are 0.5 cm thick and the E blocks on each arm have a total thickness of 30 cm. This is achieved in a single block on RA and by stacking two 15 cm thick blocks one behind the other on RB. With a total thickness of 30.5 cm and taking range straggling into consideration, protons of up to $\approx$ 220 MeV can be stopped within the active material. The front RB blocks can stop protons of up to $\approx$ 149 MeV while protons with higher energy pass through and stop in the blocks behind. We thus have a mixture of stopping and transmission spectra, each presenting a different light output. Two MWPCs, spaced 12.7 cm apart, are placed in front of the ΔE counters on each arm to provide particle location on the X and Y planes, with an intrinsic resolution of 1 mm along the scattering plane X and 2 mm in the Y plane. These MWPCs have an active area of 15.0 x 15.0 cm^2. The performance of these counters is characterized by a 2.8% resolution in $\Delta E/E$ translating to 1.6% in $\Delta P/P$ for a summed proton energy of 304 MeV for the two arms[23].

2.3 The Tel Aviv Bars, TA and TB

Each Tel Aviv arm (TA, TB) consists of a two plane (X and Y) 15.0 x 15.0 cm^2 MWPC, a thin ΔE scintillator (0.5 cm) and an array of eight $12.5 \times 10.0 \times 100.0\,cm^3$ long scintillator bars arranged in the vertical direction and viewed by a photomultiplier tube (PMT) at each end. The ΔE counters (connected to one PMT) were used in the hardware trigger in order to veto neutral particles. These counters were positioned at a distance of 15 cm from the target, while the MWPCs were at 26.5 cm with the arrays located at 200 cm from the target. The trajectory of a charged particle was obtained with the aid of the MWPC and by the measurement of its position in a bar. The horizontal resolution is given by the width (12.5 cm) of each bar, while the vertical position is measured by the time difference $\Delta t = (t_{up} - t_{down})$ of a particle's signal from either end of the bar. Each one of the Tel Aviv arms subtended a solid angle $\Delta\Omega \approx 0.25$ sr.

3. ANALYSIS

3.1 Absolute Normalization

The number of beam particles, S_{beam}, was recorded by requiring a coincidence Hodo·S1 between the hodoscope (Hodo) and the scintillator S1. To obtain the number of pions, N_{π^+}, impinging on the target, two corrections are applied: 1) The M11 pion beam is contaminated by muons, electrons and protons. The pion fraction of $f_{\pi^+} = 98.2$ % was taken from a previous measurement[24]. 2) At our beam rate of a few MHz one has to correct for the number of multiple pions per beam bucket, as the coincidence of the hodoscope with S1 counts at most one particle per beam bucket. This correction factor $f_d = -\ln(1-\epsilon)/\epsilon$, where ϵ =rate/rf, depends on the beam flux (rate) and on the radio frequency (rf) of the cyclotron (23 MHz). At a beam flux of 4 MHz we obtain $f_d = 1.10$. Thus the corrected number of incident π^+ was given by $N_{\pi^+} = f_d \cdot f_{\pi^+} \cdot S_{beam}$.

No off-line correction was required to account for protons in the beam because most of them were removed from the beam by inserting an absorber in between the

first and the second M11 bending magnets. The remaining protons were suppressed in the hardware trigger by imposing an upper threshold on the S1 signal. Effectively pions, muons and electrons were counted and signalled a trigger from the beam.

The areal density of the liquid ^{4}He target is $\sigma_o = 1.6 \cdot 10^{23}$ nuclei/cm^2. The CPU efficiency was 100 % for all triple-coincidence runs (MLU=3), which had an event rate of a few Hz only.

Full differential cross sections $d\sigma/d\Omega$ ($\pi^+ d \rightarrow pp$) were measured with a liquid D_2 and a solid CD_2 target to check the absolute normalization. As this introduces another target of different physical size along the beam axis, only the beam normalization can be checked. The data were analyzed in various ways to systematically investigate the side-effects of reaction losses, edge effects, and chamber efficiencies. The extracted angular distributions agreed with published data within 5 to 10 %. Therefore, we assumed conservatively a 10 % overall normalization uncertainty given that the areal density of the target is well known.

3.2 Energy calibration of RA and RB

The principle of the calibration was to enable energy determination for all particles stopping in the detector. To perform appropriate light summation from ionizing particles the different gains from each PMT were determined as well as the ADC offsets. The light response was linear over a wide energy range (70 to 200 MeV) and behaved at lower energies as is expected for plastic scintillators. To obtain the proton energy at the target reaction vertex, the ionization losses in the target materials, air, MWPC, windows and ΔE-counter were included. For details the reader is directed to Ref.[25].

As a representative result of the calibration, a proton energy spectrum from the $\pi^+ d \rightarrow pp$ reaction is displayed in Fig. 3 for RA=43.7°. The energy spectrum is given in the 2N center of mass system in order to suppress kinematical broadening due to the acceptance bite $\Delta\theta_{RA}$. A resolution of 5% (FWHM) was achieved at T_p^{CM}=150 MeV, which corresponds to T_p^{lab}=193 MeV lab frame kinetic energy. Besides the monoenergetic peak at T_p^{CM}=150 MeV, a tail to the left side of the peak extends down to the detection threshold. This tail results from protons which underwent a nuclear reaction in the scintillator before depositing their entire kinetic energy in the scintillator. The energy is lost due to out-scattering of the protons (elastic scattering), nuclear excitation followed by radiative de-excitation, p-n charge exchange scattering etc. With the use of a liquid D_2 target, the reaction losses were studied free of background. The solid angle of the counters was constrained by means of the MWPCs to avoid interference of reaction losses and edge effects, which both contribute to the tail to the left of the monoenergetic peak. Protons from the $\pi^+ d \rightarrow pp$ reaction were selected in the coincident counter for the second proton and any protons with the correct ΔE were accepted from the counter under investigation. The resulting proton energy spectrum (Fig. 3) reflects the ratio of the reaction tail to the peak.

3.3 Calibration of TA and TB

The calibration of TA and TB comprises three pieces of information: 1) time-of-flight (TOF), 2) vertical position (TDIF) and 3) pulse-height (PH).

The kinetic energy of an incident charged particle is calculated by means of the

measured time-of-flight and the associated flight path length from the target to the detector array. The TOF for each bar is given by the mean time of t_{up} and t_{down}, $TOF = 1/2 \cdot (c_{up} \cdot t_{up} + c_{down} \cdot t_{down}) - offset$, where c_{up}, c_{down} are constant gains (50 ps/ch) of the TDCs and the offset (time zero) is the quantity to be calibrated. All TDCs were started by the small in-beam counter S1. In order to avoid broadening due to different path lengths, the calibration was constrained to events in the middle of each bar. This was accomplished by imposing a narrow vertical acceptance on the coincidence counters (RA or RB) on the opposite side of the beam. In addition, the energy loss of the calibration protons was calculated in all material layers between the target and the scintillation bars. The effective TOF, which includes energy loss, was used to determine the offset of each bar. In Fig. 4, a time-of-flight spectrum obtained in TA from the $\pi^+ d \rightarrow pp$ reaction is displayed, where a resolution of ΔTOF=0.54 ns (FWHM) was achieved. During data analysis the impact position for each particle was calculated from the vertical position and bar number, which allowed a precise distance determination between the target vertex and the TA and TB counters.

The resolution and linearity of the vertical position in a bar, $TDIF = L \cdot (c_{up} \cdot t_{up} - c_{down} \cdot t_{down}) - offset$, were investigated using a thin "finger" counter in front of a bar and demanding a coincidence between the small counter and the bar. The small scintillator was displaced in steps of 10 cm over the entire length of the bar. A completely linear response between the vertical position and the TDC difference between the two ends of the bar was found. The position resolution is 6 cm (FWHM), determined by the combined resolution of t_{up} and t_{down}. The light propagation velocity L in the bar amounts to 14 cm/nsec . This translates to an angular resolution of 2^0 (FWHM) in ϕ with respect to the target. The standard procedure to perform the position calibration (offset) was to analyze time difference spectra of events where the counters TA, TB were fully illuminated by reaction particles originating from the target.

The thickness of the bars (10.0 cm) limits the maximum energy for stopping protons to 117 MeV. Hence the pulse-height information was not converted to particle energy, as many particles did not stop in the scintillator array. However, for a unique particle identification the pulse height was inter-calibrated among all the bars using the geometrical mean of the pulse heights, $PH_{bar} = c\sqrt{(PH_{up} - offset) \cdot (PH_{down} - offset)}$, determining the ADC-offsets for each individual PMT and a common gain c for each bar.

3.4 Data Reduction and Diagnostics of Calibration Stability

The good three-proton events originating from the ^{4}He target are extracted by means of the following cuts: 1) Proton identification and separation in three detectors; 2) two-dimensional cut on the target region from the vertex reconstruction of the trajectories and 3) cut on the missing mass distribution. All data are treated in the same manner regardless of the MLU trigger level, because the mass cut on protons in three detectors is equivalent to a triple coincidence.

The proton identification and separation was imposed in two-dimensional $\Delta E - E$ plots for RA and RB, and in $\Delta E - E$ as well as in TOF-E plots for TA and TB. The proton bands are well separated from scattered pions and reaction deuterons. Two-dimensional box cuts were defined for RA (Fig. 5) and RB in such a way that protons

which underwent nuclear reactions within the scintillator material or which escaped through the sides were rejected, because the correct energy could not be determined. The box cuts for TA, TB were defined differently. All protons were accepted, as the energy is computed by means of TOF where stopping of the particles in the scintillator is not required (Fig. 6). Protons with kinetic energy $T_p > 120$ MeV passed through the scintillator and therefore the pulse height E_{TA} tips over for protons with short TOF. All deuterons stopped in the scintillator bars and thus no ambiguity between protons and deuterons occurred. To separate the fastest protons and pions, box cuts were imposed on both TOF-E and ΔE-E distributions.

The trajectory for all detected particles was reconstructed. The two MWPCs defined the trajectory of particles in RA and RB. The bar number and the vertical position together with the MWPC defined the trajectory for TA and TB. For each event the reaction vertex was calculated by minimizing its distance to the three trajectories. Position resolution of the MWPCs and the bars was taken into account. The X-, Y- and Z-projections of the target vertices are displayed in Fig. 7, where X and Y reflect the beam distributions, folded in with interaction probability and vertex resolution. The Z-distribution allows a cross-check of the target thickness. A two-dimensional cut was imposed on the target region in the X-Z plane by which all background events from the in-beam scintillators and the target windows were rejected except those from the target flask.

The kinematical completeness of the experiment allowed the determination of the missing mass M (Fig. 8). The resulting distribution peaked around the neutron mass as expected for the ^{4}He(π^+, ppp)n reaction. The resolution of the missing mass distribution is 20-25 MeV (FWHM) for most of the runs. A small rather flat background remained on both sides of the peak which can be attributed to competing processes in the target flask. As a result, background rejection was judged to be so effective that empty target measurements were not necessary.

To monitor the stability of the energy calibration a software diagnostic program was developed making advantage of the completeness of the reaction kinematics. Two-dimensional plots of the kinetic energy spectra (T_p(RA), T_p(RB), T_p(TA), T_p(TB)) vs. the missing mass M were produced to check the constancy of M=M_n (the neutron mass) over the entire energy range in the three detectors. A projection of such plots was displayed in Fig. 8. The TOF of TA and TB turned out to be extremely stable while gain shifts occurred in RA and RB. Those were identified and consequently the gain factors were adjusted iteratively until M=const. was achieved simultaneously for all three proton energy spectra over the entire dynamical energy range. Hence this diagnostics represents a powerful tool to ensure the energy calibration.

3.5 Monte Carlo Simulation

In order to interpret the data, a MC code generated either three-nucleon or four-nucleon phase space[26]. The generation of 4N phase space is straightforward, while the 3N phase space of a quasifree 3N cluster in ^{4}He is obtained by weighting the 4N phase space with the momentum distribution as measured in electron scattering ^{4}He(e,e'p)[27]. The weight of each event was determined by the probability of a nucleon in ^{4}He to have the particular momentum of p_4 (spectator nucleon). The geometry and the energy threshold ($T_p > 38$MeV) of all four detectors were defined in the MC program allowing for a realistic comparison of any observable between experiment

and MC calculation. To obtain integrated cross section information, the acceptance of the detector system, G_A, was calculated for each configuration and for both 3N and 4N processes. G_A is defined as the ratio of the number of valid triple coincidences to the total number of trials. Typically $5{\cdot}10^7$ events were generated isotropically in 4π for each angle setting. The acceptance values for the three-nucleon absorption, G_A^{3N}, are $\sim (1-2) \times 10^{-4}$ at the peak (see Table 2) with a small statistical uncertainty. The uncertainty from the proton detection thresholds limits the knowledge of the acceptance to $\sim$ 10%. G_A^{3N} depends strongly on the relative angle of the three detectors and it changes by one order of magnitude when one counter is displaced by $\sim$ 30 degrees from the peak. The acceptance values for the four nucleon absorption, G_A^{4N}, are smaller in the region where G_A^{3N} peaks but do not exhibit a rapid change with the counter configuration (see Table 2).

The MC calculations were compared to another code, which is more efficient because events are not generated in 4π. With this code, which is described elsewhere[17] the implication of the choice of momentum distribution on the proton energy spectra was investigated. Apart from using the electron scattering data, an exponential momentum distribution of the form $\exp(-0.5(p/p_{Fermi})^2)$, where p_{Fermi} was varied around a mean value of 65 MeV/c, was applied to the four-body phase space to produce the quasifree three-body phase space. The differences are minor for reasonable choices of momentum distributions. In any case, the knowledge of the spectral shape obtained from three-body MC calculations is strictly limited by the lack of experimental data on the neutron momentum distribution in ^{4}He and by the applicability of the quasifree model in pion absorption. This MC code was also used to simulate deviations from the four-body phase space, e.g. final state interactions of outgoing nucleons.

3.6 Cross sections

In this experiment the results are presented in terms of multiple (three- or four-fold) differential cross sections and in integrated form.

The energy integrated three-fold differential cross section is defined by

$$\frac{d^3\sigma}{d\Omega_1 d\Omega_2 d\Omega_3} = \frac{N^{3p}}{N_{\pi^+}\sigma_o \Delta\Omega_1 \Delta\Omega_2 \Delta\Omega_3 \epsilon} \tag{1}$$

where N^{3p} is the number of three proton events, N_{π^+} and σ_o are defined in section 3.1, and $\Delta\Omega_{i,i=1,2,3}$ are the solid angles for the detectors being 0.25 sr for TA and TB each (or $\sim$ 0.031 sr for each bar), and 0.148 sr and 0.144 sr for RA and RB respectively. The parameter ϵ is the combined efficiency of all MWPCs and the correction for the reaction losses in RA and RB which are energy dependent. The angular distribution $d^3\sigma(\theta_{p_3})/d\Omega_1 d\Omega_2 d\Omega_3$ of protons p_3 for constant angles of protons p_1 and p_2, the momentum distribution $d^4\sigma(p_n)/d\Omega_1 d\Omega_2 d\Omega_3 dp_n$ of the undetected neutron, and the kinetic energy distributions $d^4\sigma(T_{p_i})/d\Omega_1 d\Omega_2 d\Omega_3 dT_{p_i}$ of the three detected protons $p_{i,i=1,2,3}$ are the observables providing information on the reaction mechanism. These distributions were compared with the MC distributions.

To estimate the total cross section for three proton emission (σ^{3N}) the differential distributions $d^3\sigma/d\Omega_1 d\Omega_2 d\Omega_3$ were integrated over 4π by extrapolation into unmeasured regions of the phase space. The MC calculations provide the ratio of

the measured to the unmeasured portion of the phase space (acceptance G_A^{3N}) for three protons in the selected counter configuration. The integrated cross section σ^{3N} is therefore given by

$$\sigma^{3N} = \frac{N^{3N}}{N_{\pi+}\sigma_o G_A^{3N}\epsilon} \tag{2}$$

where $N_{\pi+}$, σ_o and ϵ are the same numbers as used in Eq. (1), and G_A^{3N} is the acceptance as defined in section 3.5. Correspondingly, the integrated cross section for four-nucleon absorption can be estimated with

$$\sigma^{4N} = \frac{N^{4N}}{N_{\pi+}\sigma_o G_A^{4N}\epsilon}. \tag{3}$$

The number of events N^{3N} and N^{4N} were determined for each configuration separately. The results of the integration will be described in section 4.3 together with more detailed information on how N^{3N} and N^{4N} are obtained.

4. RESULTS AND DISCUSSION

4.1 Differential cross sections

The kinematic completeness of the present triple-coincidence experiment allows full reconstruction of each event and is therefore very sensitive to the pion absorption reaction mechanism leading to multi-nucleon emission. Experimental distributions are compared to MC calculations with different reaction mechanism. For this purpose, angular correlations $d^3\sigma(\theta_i)/d\Omega_1 d\Omega_2 d\Omega_3$, missing momentum distributions $d^4\sigma(p_n)/d\Omega_1 d\Omega_2 d\Omega_3 dp_n$, and proton energy spectra $d^4\sigma(T_{p_i})/d\Omega_1 d\Omega_2 d\Omega_3 dT_{p_i}$ seem to be most conclusive and hence are described below.

Angular correlations $d^2\sigma(\theta_2)/d\Omega_1 d\Omega_2$ were already studied in the case of 2NA as mentioned in the introduction. It is clear that angular correlation distributions are also sensitive to more complicated mechanisms, because the selection of three detector angles, together with the energy threshold of the detectors, reduces the available phase space for three nucleons considerably more than for four nucleons. Hence some counter configurations favour three-nucleon phase space while others can only be populated by four-nucleon emission. This phase space selectivity provides the sensitivity necessary to distinguish between different reaction mechanisms. The angular correlations were investigated by measuring the angular distribution of protons over a wide range in TA and TB for fixed angles of the two other detected protons (RA,RB). In Fig. 9a-c the angular distributions of protons detected in TA or TB are exhibited for fixed angles of RA=40^0 and RB=106^0 (Fig. 9a), RB=121^0 (Fig. 9b), and RB=136^0 (Fig. 9c) respectively. All data displayed are from RA · RB · TA or RA · RB · TB coincidences, because in such a way an almost continuous angle coverage is obtained between 25^0 and 140^0. This information is not as complete for RA·TA·TB or RB·TA·TB coincidences. Most of the data result from measurements with MLU=3 (solid dots). Only for RB=106^0 the angle distribution was complemented with MLU=2 (open circles) measurements. Many of the MLU=3 runs were repeated and some of the measurements were also taken with MLU=2 for consistency. All data points are absolutely normalized with a combined MWPC efficiency $\sim$ 70% (typically), 100 %

CPU efficiency for MLU=3, and 10-20 % corrections for reaction losses in RA and RB. The data are consistent with each other. A subset of these data has already been published elsewhere[28]. The proton distributions in Fig. 9a-c peak at $\sim 81^0$, 72^0, and 63^0 with RB being at 106^0, 121^0, and 136^0, respectively, and on both sides of the peak the cross section drops rapidly. The shift in the peak position indicates clearly the correlation with the angle of the detector RB. The distributions are compared to the respective MC simulations for 3N and 4N phase space as discussed in section 3.5. All curves are normalized to the peak of the measured distributions for best shape comparison with the data. This was achieved with normalization constants, which agreed with one another within $\pm 10\%$. The 3N simulations follow the data in the region of the peak much better than the 4N simulation but do not extend to the very small and large proton emission angles. Hence, we conclude that the data in the peak are obtained from pions interacting with three nucleons $\pi^+ppn \rightarrow ppp$ and the very small fraction of events in the tails of the distributions might involve four nucleons via $\pi^+\alpha \rightarrow pppn$.

The momentum distribution of the undetected neutron

$$p_n = \mid \vec{p}_\pi - \sum_{i=1,2,3} \vec{p}_i \mid , \tag{4}$$

is shown in Fig. 10 for the configuration with RA=40^0, RB=136^0, and TA=-55^0. This configuration is chosen to be in the peak region of Fig. 9c, where the 3N process dominates according to the MC calculations. The missing momentum distribution in Fig. 10 peaks at $\sim$ 100 MeV/c with a small hump at 300 MeV/c. For comparison the MC simulations for 3N and 4N phase space are drawn as solid curves. The agreement of the experimental spectrum with the quasifree 3N phase space calculation is very good in the momentum region 0-200 MeV/c which covers a large fraction of the events in the spectrum. The 4N phase space distribution is broader with a maximum around 200 MeV/c and fails to explain the data in the low-momentum region. This provides strong evidence that the three-proton coincidences at this configuration result mainly from the reaction of a pion with three nucleons, which supports the conclusion drawn from the angular correlations (Fig. 9a-c). However, the enhancement around p_n=300 MeV/c cannot be explained by the 3N phase space calculation. The occurrence of this bump is probably due to an interaction of a pion with four nucleons since the four-nucleon phase space extends to this momentum region.

The neutron momentum distribution of Fig. 10 can be directly compared to the experiment at T_π=120 MeV[22], where the momentum distributions of the undetected nucleons were displayed for both reactions ^{4}He(π^+, ppp)n and ^{4}He(π^+, ppn)p. There, the relevance of the spectator momentum distribution on the reaction mechanism was already demonstrated with similar conclusions although the peak for p_n(^{4}He(π^+, ppp)n) at 300 MeV/c was almost as pronounced as the peak around p_n=100 MeV/c. In Ref.[22] the second bump was explained by the special geometry of the three detectors which favoured soft final state interaction (FSI) of a pair of outgoing nucleons with small relative momentum following pion absorption on four nucleons. Our data do not reveal such a strong effect of FSI which facilitates the interpretation of the data. One reason for the less pronounced effect might be that the kinetic energy released to each proton from the reaction ^{4}He(π^+, ppp)n (the neutron being essentially a spectator) is

on the average almost 100 MeV (total pion energy $E_\pi \sim 305$ MeV) and all detector thresholds are set to 38 MeV. Hence more protons are detected far above the energy threshold and less low-energy protons are detected that can be involved in final state interactions.

Proton energy spectra measured in RA, RB, and TA are presented in Fig. 11a-c for the same geometry as in Fig. 10. The solid curves labelled "3N" and "4N" denote the respective MC phase space calculations and are normalized to the peak of the data. The dashed curve in Fig. 11c is identical with the 3N phase space curve but the TA energy axis is scaled by 0.92 to match the shape of the experimental spectrum. The comparison of the proton kinetic energy spectrum T_p(TA) in Fig. 11c with the shape for 3N and 4N phase space reveals the sensitivity of this variable to the reaction mechanism. The measured spectrum - broadened by the $\sim$ 0.5 nsec TOF resolution - agrees well with the dashed 3N phase space curve apart from the low-energy tail which is not compatible with 3NA. The majority of events is within the acceptance of 3N phase space. In contrast, the proton energy spectra as measured in RA and RB (Fig. 11 a,b) do not exhibit a similar sensitivity to the reaction mechanism for this particular geometry because both phase space curves peak in the same energy region. However, the 3N MC calculation reproduces also the data for RA and RB better than the 4N MC calculation. Hence qualitative agreement is obtained between the data and the 3N MC calculation for all three energy spectra of Fig 11a-c. The sensitivity of the TA energy spectrum (Fig. 11c) to the reaction mechanism is related to the configuration, i.e. the relative angle between the detectors. For other configurations with RA · TA · TB coincidences the energy spectrum of RA looks very similar to the one of TA in Fig. 11c.

The configurations listed in Table 1 were analyzed for all possible trigger combinations, i.e. RA·RB·TA, RA·RB·TB, RA·TA·TB, and RB·TA·TB coincidences. The obtained information is extensive. The angular information is largely displayed in Fig. 9a-c, although this is just one way to present the data. We also compared the angular distribution of protons measured in RB at 106^0, 121^0, and 136^0 for fixed angles of RA and TA. The agreement of this distribution with the 3N MC calculation is good. The energy information from RA, RB, TA, and TB as well as the missing momentum distribution for each configuration cannot be plotted in such a compact manner and are beyond the scope of this paper. However, further information is provided in Fig. 12 for three more configurations, which demonstrate the impact on the energy spectra when only one detector is displaced (RA=40^0, TA=-70^0, and a) RB=136^0, b) RB=121^0, and c) RB=106^0). At first glance, the corresponding spectra look all very similar and also comparable to Fig. 11a-c. However, for the detailed understanding of the reaction mechanism subtle differences in the shape can be important as will be emphasized in section 4.2 when competitive processes leading to three-proton final states are discussed.

The missing momentum distribution and the proton energy spectrum T_p(TA) displayed in Figs. 10 and 11c largely demonstrated the dominance of 3N cross sections over a 4N mechanism. However, both figures have a common feature, namely that a part of the experimental spectrum is not explained by the three-body MC calculation suggesting another contribution, which might be due to 4N absorption. For a thorough understanding of the spectra in Figs. 10 and 11c, it is important to know whether the regions of incompatibility with the three-body MC correspond to one

another. Therefore, we investigated the correlation of these distributions by analyzing the data with additional cuts imposed on the proton energy spectrum $T_p(TA)$ and looking at the missing momentum distribution of the remaining events. The same data as displayed in Figs. 10 and 11c were investigated with the energy intervals $38 < T_p(TA) < 70$ MeV, $38 < T_p(TA) < 90$ MeV, $38 < T_p(TA) < 110$ MeV, and $100 < T_p(TA) < 180$ MeV. The missing momentum distributions for these energy intervals are plotted in Fig. 13a-d. The low-energy tail of $T_p(TA)$ is obviously correlated with a missing neutron momentum of 300 MeV/c and largely explains this bump. On the other hand, the missing momentum distribution of the energy interval $100 < T_p(TA) < 180$ MeV does not have any component at 300 MeV/c and coincides with the 3N MC calculation. Consequently the low-energy region of $T_p(TA)$ was further investigated. Several approaches were attempted with the MC technique, one of which is a 2NA process with the additional detection of a proton with high Fermi motion. More promising were the simulations of 3N or 4N phase space calculations including soft FSI, where the matrix element is enhanced for events with nucleons having very little relative momentum[17]. Qualitative agreement was achieved for the low-energy part of $T_p(TA)$ and the high-momentum region of the missing momentum distribution with a 4N phase space simulation accompanied by soft FSI. This conclusion is in agreement with Ref.[22].

So far experimental data were compared to MC "events" with the emphasis of discussing the shape of different MC calculations from which the prevalence of 3NA was inferred. An important aspect is also the more quantitative question of whether the 3N phase space calculations can be normalized to the spectra of different configurations with one common normalization constant. The constancy of this number is a direct measure of the uniformity of the 3N process. The angular distributions presented in Fig. 9a-c demonstrate that there is some dependence of the triple-differential cross section on the angle of RB. However, the MC calculations show a similar behaviour in which case the dependence is given by phase space only. The 3N curves in Fig. 9a-c were obtained with normalization constants which differed by $\pm 10\%$. Uniformity will be assumed when the data are integrated to obtain the total 3NA cross section. Therefore the issue of constant normalization and uniformity of the 3NA process will be raised again when the data are integrated in section 4.3.

4.2 Reaction mechanism

The angle correlations, the missing momentum distributions, and the energy spectra of the three-proton coincidences all combine to provide strong evidence that pions are absorbed in a reaction with three nucleons, yet the details of the reaction mechanism remain uncertain. The three-nucleon absorption $\pi^+ppn \rightarrow ppp$ is genuine if the pion is absorbed by three correlated nucleons in one step. In the simplest case, the cross section is proportional to three-nucleon phase space with a constant matrix element. Several diagrams with one or two Δs in the intermediate state have to be considered as possible reaction mechanisms[1]. No differential distributions from microscopic calculations exist to date for such 3N diagrams, probably because of lack of experimental evidence.

We examined all proton energy spectra in the regions of 3N dominance and observed a trend which agrees with the discussion of Fig. 11a-c. The proton energy spectra agree qualitatively with the shape of the 3N phase space, if the energy axes

are scaled (or shifted) appropriately. This feature is not easy to explain. Obviously genuine 3N absorption can exhibit a more complicated form than just proportionality to 3N phase space but as mentioned above there are no theoretical calculations to compare with. The possibility that instrumental reasons are responsible for the observed behaviour of the energy spectra has also been investigated. An alignement problem or an error in the energy calibration could conceivably create the same effect. The latter, however, seems rather unlikely due to the careful calibration checking as described in section 3.4.

There are at least two other reaction mechanisms leading to three nucleons in the final state. Both are two-step processes, one of which is two-nucleon absorption. Hence these reaction mechanisms are not compatible with a genuine three-nucleon absorption. If pions are scattered off a single nucleon prior to 2N absorption (ISI+2NA) or if a nucleon following 2NA is interacting with another nucleon (2NA+FSI), three nucleons are emitted which could falsely be interpreted as "three-nucleon" absorption. Although the experimental signature might be quite similar to genuine 3NA in certain regions of phase space, the basic reaction mechanism leading to three-nucleon emission is totally different. Therefore it becomes an important issue to distinguish between genuine 3NA and two-step processes.

A signature for initial state interactions and final state interactions was reported by Ref.[20] in the (π^-, pp) reaction. An experiment looking specifically for two-step processes by measuring three protons from the reaction $^{12}C(\pi^+, ppp)X$ in coincidence came to the opposite conclusion[16]. It was also suggested, that ISI prior to 2NA would shift the peak position of 2N angular correlations[29], but no such observation was reported to date. Recently $^3He(\pi^+, pp)p$ data recorded far away from the 2NA region were analyzed to investigate the nature of three-nucleon emission[30]. A one-step genuine three-nucleon absorption explains the data using a model in which the mass distribution of the exchange meson in the intermediate state is sensitive to the reaction mechanism[31]. Without referring to this model, in which Fermi motion is neglected, our differential distributions are examined to address this question qualitatively. It is clear that the missing momentum distribution does not help in this case to delineate the reaction mechanism. The p_4 distribution is useful to distinguish between 3N and 4N mechanisms but cannot separate different reaction mechanisms involving three nucleons. The angular correlations are certainly sensitive to the reaction mechanism, but MC calculations of two-step processes ISI+2NA and 2NA+FSI are required for a realistic analysis, representing a difficult task with many uncertainties which we avoided. The energy spectra seem to be more useful for a qualitative discussion.

When a pion is scattered off a single proton in a quasifree process then the proton is observed with a strong energy-angle correlation. For instance, if binding energy is neglected the proton energy measured in RA=40^0 would be $\sim$ 50-55 MeV (or $\sim$ 30-35 MeV in TA=-55^0), broadened by the acceptance of the detector and Fermi motion. Consequently the pion is back-scattered with $\sim$ 110 MeV at -(80-85)^0 (or $\sim$ 135 MeV at 55^0) and when absorbed in a conventional 2NA process the two emitted nucleons should be strongly correlated in energy and angle. Protons from quasi-elastic pion scattering emitted at -55^0 would be just in the region of the energy threshold of TA and cannot account for the measured energy spectrum of Fig. 11c. Less obvious is the situation for protons emitted at 40^0 and detected in RA. The RA spectrum of

Fig. 11a peaks at 50-55 MeV and extends up to 100 MeV. If the protons detected in RA were due to quasi-elastic scattering the protons detected in TA and RB would come from 2NA of 110 MeV pions scattered at 80-85^0 and would therefore show a strong correlation. Taking the finite acceptance of RA into account and allowing for large Fermi momenta in ^{4}He, such a picture cannot be ruled out. In Fig. 14a an energy plot of T_p(TA) vs. T_p(RB) is displayed. The events are distributed over the entire region allowed by phase space with a higher density at T_p(RB) $\sim$ 80 MeV and T_p(TA) $\sim$ 130 MeV. This event correlation though is not as pronounced as observed for pp-coincidences at quasifree geometries[32]. The energy plot is compared to the corresponding MC phase space simulation which shows a similar enhancement though less intense in the same region (Fig. 14b). The angle correlation θ(TA) vs. θ(RB) was analyzed as well but it is not any more conclusive. From quasi-elastic π^+p measurements it is expected that most of the protons would be detected at angles smaller than 40^0. The angular distribution of protons in RA was analyzed and it was found that more events are detected at small angles. However, events are spread over the whole acceptance of RA and the MC 3N phase space distribution behaves similarly. More information comes from Fig. 12, where the energy spectra are displayed for constant angles of RA=40^0 and TA=-70^0. The detector RA is the only one which could detect a proton from quasi-elastic scattering because of the energy threshold, and consequently the energy spectrum should not change. It is observed, however, that the RA proton energy spectrum changes shape with the angle of RB, i.e. the peak position moves from $<$ 50 MeV to $\sim$ 65 MeV when RB is displaced from 106^0 to 136^0. Furthermore the proton energy spectrum extends up to 150 MeV when RB=136^0 which seems incompatible with the idea of quasi-elastic scattering but is within the acceptance of the 3N phase space calculation.

Now we consider the case of 2NA+FSI where we can make the reasonable assumption that only one of the emitted nucleons is involved in final state interactions, i.e. knocking out another nucleon. This means that one proton preserves the energy from the 2NA process whereas the energy of the other nucleon is altered due to scattering from a third nucleon. Furthermore, kinematics dictate that the opening angle between the two nucleons involved in the final state interaction is $\sim$ 90^0 because of their equal masses. Also, the energy spectra of these two protons must be correlated because the sum of the two kinetic energies is constant apart from Fermi motion for a given angle of the proton which is not involved in FSI. We consider the same geometry with RA=40^0, RB=136^0, and TA=-55^0. The kinetic energy of a proton from 2NA emitted at -55^0 is $\sim$ 160-165 MeV (at 136^0 $\sim$ 80-85 MeV). Referring to Fig. 11a-c, the proton energy spectra of RA and TA are not compatible with an unaltered proton spectrum from 2NA. Only the proton energy spectrum of RB comes close to what is expected from 2NA, in which case angular and energy correlations would be seen between RA and TA. In Fig. 15a the energy plot of T_p(TA) vs. T_p(RA) is displayed, and in Fig. 15b is the corresponding MC plot obtained with 3N phase space. No correlation in the data is visible apart from the one which was mentioned in Fig. 14a. Also the angle plot θ(TA) vs. θ(RA) was investigated giving no indication for correlated protons. Further evidence against the two-step mechanism 2NA+FSI can be inferred from the sensitivity of the proton energy spectrum RB when the angle of TA is varied. Also the peak position of the angular correlation (Fig. 9a-c) moves when the angle of RB is changed from 136 to 106 degrees, in contrast to the acceptance of RA and TA

which is restricted to $\sim 90^0$ opening angle for a nucleon undergoing scattering with another nucleon.

In conclusion, a 3N phase space process seems necessary to explain our data because all energy and angle regions allowed by 3N phase space are populated. The form of the matrix element, however, is yet not clear because the 3N phase space calculations do not match exactly the measured proton energy spectra. On the other hand, two-step processes alone like ISI+2NA or 2NA+FSI seem to fail to explain our data. However, from our above qualitative discussion at least the process ISI+2NA cannot be discarded. Hence this two-step mechanism must be considered on the level of admixing/interfering with the genuine three-nucleon absorption. This could of course explain the discrepancies observed between the data and the 3N phase space MC. Their relative strength remains unknown. In addition, it is possible that the presence of off-shell effects and other medium modifications may distort the πN and NN interactions to the point that they can imitate genuine 3N absorption. Clearly there is a need for studies of the medium effects in realistic models of DWIA involving both entrance and exit channel distortions.

4.3 Integrated cross sections

In order to obtain the fraction of σ^{3N} (Eq.2) to the total absorption cross section in ^{4}He, one has to integrate over the unmeasured portion of the 4π space, which is either not covered by the solid angle of the detectors or is below their energy thresholds. For that purpose, the MC calculations were performed over 4π space where the ratio of the number of triple coincidences to the total number of events generated defines the acceptance (see section 3.5). In Table 2 the acceptance values G_A^{3N} are listed for all configurations of interest. The fraction of events due to 3NA was determined from the total of three-proton coincidences. The missing momentum distribution (e.g. Fig. 10) is an appropriate spectrum sensitive to the 3N and 4N contributions and hence was decomposed into a component $d\sigma^{3N}$ and $d\sigma^{4N}$. The results are listed in Table 2. The decomposition is uncertain for the configurations 4,7,10,12 and 14; hence the numbers are quoted in parentheses. Assuming isotropic emission of the nucleons, according to 3N phase space, we obtain from each configuration an integrated 3NA cross section. If the 3NA cross section is uniform one expects equal cross sections from each configuration sensitive to 3NA. The cross sections of configurations 2,3,5,6,8, and 9 agree within $\pm$10% about its mean value. Statistics is a minor uncertainty because the spectra contain typically 5000 events. Larger errors are associated with the acceptance calculation (see section 3.5), the combined efficiency from the detectors, the determination of $d\sigma^{3N}$, and beam normalization. The final result σ^{3N}=4.8$\pm$1.0 mb for T_π=165 MeV is inferred by averaging over the 3NA cross sections of configurations 2,3,5,6,8,9. The result for σ^{3N} is listed in Table 3 together with 3NA cross sections for ^{3}He and ^{4}He from other experiments. Our result for σ^{3N} in ^{4}He is fairly close to the free cross section $\sigma^{3N}(^3\mathrm{He}(\pi^+,\mathrm{pp})\mathrm{p})$=3.9$\pm$0.5 mb at T_π= 120 MeV. The increase of $\sigma^{3N}(^4\mathrm{He}(\pi^+,\mathrm{ppp})\mathrm{n})$ by more than a factor of two between T_π= 120 and 165 MeV is a feature which is not expected from the energy dependence of other pion absorption cross sections, e.g. the $\pi d \rightarrow pp$ reaction[1]. The quoted error bars are, however, rather large reflecting the fact that only a small portion of 4π is measured. On the other hand, the energy dependence of σ^{3N} can be different than σ^{2N}, especially if a double-Δ mechanism is the doorway for the reaction. In fact the ratio σ^{3N} / σ_{abs}^{tot} in

^{3}He and in carbon exhibits a different energy dependence than $\sigma(\pi d \rightarrow pp)$[17].

The uniformity of 3NA is an important aspect not only when it is assumed for integration purpose but also for the understanding of the reaction mechanism. The measurements on the He isotopes seem to be controversial. The first triple-coincidence experiment in ^{4}He[22] was not sensitive enough to this question because only one counter geometry was measured. The first angular correlation study in ^{3}He[14] at T_π= 120 MeV leads to the conclusion that $d\sigma^{3N}$ is proportional to 3N phase space. An angular dependence is obtained at higher pion energies (T_π= 350 and 500 MeV)[15] and at low energies the proton energy spectra seem to follow 3N phase space whereas the cross sections at different detector angle pairs differ substantially (more than a factor of 2)[12]. Certainly the matrix element for 3NA can depend in various ways on the angle and the energy. Especially, if two-step processes contribute to the triple coincidences in ^{4}He or if the tails of 2NA with high spectator momentum components extend into the measured two-fold coincidences in ^{3}He, deviations from phase space must be expected. The observed ratio of $\sigma^{3N}(^4\text{He}(\pi^+,\text{ppn})\text{p})/\sigma^{3N}(^4\text{He}(\pi^+,\text{ppp})\text{n}) \sim 2$ by Ref.[22] is another interesting feature of three-nucleon absorption. Spin- and isospin quantum numbers of the initial and final NNN-state affect the cross section. The energy and isospin dependence of three-nucleon absorption pose challenging features which need to be explained by theoretical calculations. Detailed calculations do not exist to date. Recently the formation of a πNN resonance as doorway for three-nucleon absorption was suggested[33]. Oset et al.[34] investigated the energy dependence of integrated 2N and multi-nucleon pion absorption and found that 3NA becomes important at resonant and higher energies whereas 4N remains negligible. A completely different attempt was made by Barshay[35] who incorporated quark degrees of freedom. A three-nucleon force was explicitly built-in, mediated by the wandering of quarks between three neighboring nucleons. This calculation represents a completely different picture than conventional π-3N interaction. Surprisingly, qualitative agreement was achieved for the integrated cross sections and the differential cross sections would be proportional to phase space in this model. A cross section with almost constant matrix element, depending only on the pion kinetic energy, might be difficult to obtain with intermediate double-Δ formation in the mesonic calculations.

The 4NA cross section σ^{4N} (Eq.3) was estimated similarly to 3NA assuming isotropic emission of the nucleons according to 4N phase space. The acceptance for three protons constrains the small and large angle regions of the triple-differential cross sections (Fig. 9a-c) to exclusively 4N phase space, whereas in the region where the measured distributions peak both 3N and 4N phase space are available. Hence 4NA cross sections were determined free from any 3NA contribution at small and at large angles. However, the event statistics is poor to investigate differential distributions because the 4N phase space is so small there. In addition, the missing mass cut described in section 3.4 is not suppressing the background sufficiently at such a small event rate. The background manifests itself in the proton energy spectra at energies disallowed by 4N phase space. Alternatively in the angle region of larger phase space the analysis of 4NA suffers from a reliable determination of $d\sigma^{4N}$, as the events are dominated by $d\sigma^{3N}$. Furthermore, $d\sigma^{4N}$ is likely to be enhanced due to FSI as discussed in section 4.1. The relevant information for all configurations is given in Table 2. We conclude that the 4NA cross section $\sigma^{4N} < 2$ mb. An upper limit is given because the cross section is likely to be overestimated due to soft FSI[22],

some background and possibly some 3N+FSI contributions. The result for σ^{4N} is also compiled in Table 3 for direct comparison with the measurement by Backenstoss et al. at T_π=120 MeV[22]. The 4N cross section σ^{4N} seems to be negligible for total pion energies $E_\pi < 300$ MeV in ^{4}He. This is a very important result because the process of four-nucleon emission was suggested by Brown et al.[36]. In their model the pion is absorbed via intermediate double-Δ formation, where each Δ decays in a $\Delta N \rightarrow NN$ interaction. This mechanism was disputed by Oset et al.[34]. However, to test the calculations of Ref.[36] at higher energies, measurements with $T_\pi > 200$ MeV are needed in addition.

The integrated 3N cross section, σ^{3N}, is significant and amounts to $\sim 35-40\%$ of $\sigma(\pi d \rightarrow pp)$ at T_π=165 MeV. However, this corresponds to only $\sim 6\%$ of the total absorption cross section $\sigma_{abs}^{tot}(^4He) \sim$ 70-80 mb[37]. In ^{3}He a much higher percentage was reported, i.e. $\sigma^{3N} \sim 20-30\%$ of $\sigma_{abs}^{tot}(^3He)$. The rapid increase of the total absorption cross section from ^{3}He to ^{4}He is known, but the cross section for $\sigma^{3N}(\pi^+,ppp)$ seems rather constant. Even if $\sigma^{3N}(\pi^+,ppn)p > \sigma^{3N}(\pi^+,ppp)n$, as reported by[22], the absorption cross section involving more than two nucleons does not exceed $\sim 20\%$ of $\sigma_{abs}^{tot}(^4He)$ at resonance energies and therefore cannot explain the large amount of missing cross section as reported by[2]. As other absorption processes such as composite particle emission[38,39] are also small compared to the total absorption cross section, the disagreement might be the consequence of poorly determined cross sections for σ^{2N} and σ_{abs}^{tot}.

5. SUMMARY AND CONCLUSIONS

In summary, we have measured the angular correlation of three-proton events from the reaction ^{4}He$(\pi^+,ppp)n$ for several angle settings and compared the results with 3N and 4N phase space MC calculations. The majority of events falls within the acceptance of 3N phase space. The same conclusion can be drawn from the analysis of the missing momentum spectra. The proton kinetic energy spectra were analysed to explore whether protons are emitted according to 3N phase space. Only partial agreement is observed between measurement and 3N simulation. This could imply that three protons are not always emitted according to 3N phase space. Two-step processes like ISI+2NA or 2NA+FSI could be a possible additional explanation for three-nucleon emission. We have not found any evidence for 2NA+FSI. A genuine three-nucleon absorption mechanism with a matrix element of unknown structure (not constant) is an alternative. Likely we observe a combination of 3N phase space plus the two-step process ISI+2NA. In order to obtain an integrated three-nucleon absorption cross section we assumed the simplest case with a constant matrix element and get $\sigma^{3N} = 4.8 \pm 1.0$ mb.

In contrast to the results and conclusions (80-90 % missing cross section) by Ref.[2] the picture of pion absorption might have changed a little. Experiments on ^{3}He as well as on heavier targets with good excitation energy resolution suggest at least $\sim 50-60\%$ 2NA which reduces the fraction of missing cross section considerably. Data on multi-nucleon emission exist now on ^{3}He, ^{4}He, and on ^{12}C. Although the reaction mechanism leading to multi-nucleon emission is not understood, a $\sim 10-30\%$ contribution of σ^{3N} to the total absorption cross section seems to result at resonance energies, when differential cross sections are integrated (extrapolated). If there is some residual absorption strength which is unidentified, then it is most

probably associated with neutrals and/or low-energy particles, for which many of the counter experiments are not sensitive. However, it should also be mentioned that many quantitative conclusions base on total absorption cross sections with rather large error bars[40]. Most experiments provide either cross sections for a specific process (e.g. 2N, 3N, or composite particle emission) or total cross sections from transmission experiments with completely different systematic uncertainties. More precise total cross sections are very desirable as well as simultaneous measurements of differential and integrated cross sections. The role of ISI and FSI in conjunction with 2NA remains an enigma.

The now available cross sections σ^{3N} in ^{3,4}He should provide the base for theoretical calculations. For a detailed understanding of the πNNN $\rightarrow$ NNN mechanism a thorough exploration of the reactions (π^+, ppp), (π^+, ppn), and (π^+, pnn) (and the charge symmetric reactions with π^-) is highly desirable. These measurements are complicated by the necessity of neutron detection. Energy- and A-dependence pose a rather major program for investigation. With the use of a 4π detector out-of-plane measurements can be performed and the angle and energy dependence can be studied in a comprehensive manner. Phase space calculations will still be needed for interpretation but not for integration purpose.

ACKNOWLEDGEMENTS

The contribution of A. Altman, D. Ashery and M. Moinester in the planning stage of the experiment is acknowledged. The reliable target operation of the liquid helium and deuterium targets by Cam Marshal is greatly appreciated. We acknowledge the drawing skills of Pierre Amaudruz. This work was supported in part by the National Sciences and Engineering Research Council (NSERC) of Canada.

REFERENCES

[1]D. Ashery and J.P. Schiffer, Ann.Rev.Nucl.Part.Sci. **36** (1986) 207.

[2]A. Altman, E. Piasetzky, J. Lichtenstadt, A.I. Yavin, D. Ashery, R.J. Powers, W. Bertl, L. Felawka, H.K. Walter, R.G. Winter and J.v.d. Pluym, Phys.Rev.Lett. **50** (1983) 1187.

[3]A. Altman, D. Ashery, E. Piasetzky, J. Lichtenstadt, A.I. Yavin, W. Bertl, L. Felawka, H.K. Walter, R.J. Powers, R.G. Winter and J.v.d. Pluym, Phys.Rev. **C34** (1986) 1757.

[4]W.J. Burger, E. Beise, S. Gilad, R.P. Redwine, P.G. Roos, N.S. Chant, H. Breuer, G. Ciangaru, J.D. Silk, G.S. Blanpied, P.M. Preedom, B.G. Ritchie, M. Blecher, K. Gotow, D.M. Lee and H. Ziock, Phys.Rev.Lett. **57** (1986) 58.

[5]B.G. Ritchie, N.S. Chant and P.G. Roos, Phys.Rev. **C30** (1984) 969.

[6]W.R. Gibbs and W.B. Kaufmann, in Pion-Nucleus Physics: Future Directions and New Facilities at LAMPF, Proceedings of the Los Alamos Conference on Pion-Nucleus Physics, AIP Conf. Proc. 163, edited by R.J. Peterson and D.D. Strottman (AIP, New York, 1988), p. 279.

[7]R.A. Schumacher, P.A. Amaudruz, C.H.Q. Ingram, U. Sennhauser, H. Breuer, N.S. Chant, A.E. Feldman, B.S. Flanders, F. Khazaie, D.J. Mack, P.G. Roos, J.D. Silk and G.S. Kyle, Phys.Rev. **C38** (1988) 2205.

[8]R. Rieder, P.D. Barnes, B.Bassalleck, R.A. Eisenstein, G. Franklin, R. Grace, C. Mahrer, P. Pile, J. Szymansky, W.R. Wharton, F. Takeutchi, J.F. Amann, S.A. Dytman and K.G.R. Doss, Phys.Rev. **C33** (1986) 614.

[9]D. Gotta, M. Dörr, W. Fetscher, G. Schmidt, H. Ullrich, G. Backenstoss, W. Kowald, I. Schwanner and H.-J.Weyer, Phys.Lett.**112B** (1982) 129.

[10]G. Backenstoss, M. Iżycki, M. Steinacher, P. Weber, H.-J. Weyer, K.von Weymarn, S. Cierjacks, S. Ljungfelt, U. Mankin, T. Petković, G. Schmidt, H. Ullrich and M. Furić, Phys.Lett.**137B** (1984) 329.

[11]M.A. Moinester, D.R. Gill, J. Vincent, D. Ashery, S. Levenson, J. Alster, A. Altman, J. Lichtenstadt, E. Piasetzky, K.A. Aniol, R.R. Johnson, H.W. Roser, R. Tacik, W. Gyles, B. Barnett, R.J. Sobie and H.P. Gubler, Phys.Rev.Lett. **52** (1984) 1203.

[12]K.A. Aniol, A. Altman, R.R. Johnson, H.W. Roser, R. Tacik, U. Wienands, D. Ashery, J. Alster, M.A. Moinester, E. Piasetzky, D.R. Gill and J. Vincent, Phys.Rev. **C33** (1986) 1714.

[13]P. Weber, G. Backenstoss, M. Iżycki, R.J. Powers, P. Salvisberg, M. Steinacher, H.J. Weyer, S. Cierjacks, A. Hoffart, H. Ullrich, M. Furić, T. Petković and N. Šimičević, Nucl.Phys. **A501** (1989) 765.

[14]G. Backenstoss, M. Iżycki, P. Salvisberg, M. Steinacher, P. Weber, H.J. Weyer, S. Cierjacks, S. Ljungfelt, H. Ullrich, M. Furić and T. Petković, Phys.Rev.Lett. **55** (1985) 2782.

[15]L.C. Smith, R.C. Minehart, D. Ashery, E. Piasetzky, M. Moinester, I. Navon, D.F. Geesaman, J.P. Schiffer, G. Stephens, B. Zeidman, S. Levinson, S. Mukhopadhyay, R.E. Segel, B. Anderson, R. Madey, J. Watson and R.R. Whitney, Phys.Rev. **C40** (1989) 1347.

[16]R. Tacik, E.T. Boschitz, W. Gyles, W. List and C.R. Ottermann, Phys.Rev. **C32** (1985) 1335.

[17]R. Tacik, E.T. Boschitz, W. Gyles, W. List, C.R. Ottermann, M. Wessler, U. Wiedner and R.R. Johnson, Phys.Rev. **C40** (1989) 256.

[18]W. Brückner, H. Döbbeling, P.C. Gugelot, F. Güttner, H. Kneis, S. Majewski, M. Nomachi, S. Paul, B. Povh, R.D. Ransome, T.-A. Shibata, M. Treichel, Th. Walcher, P. Amaudruz, Th. Bauer, J. Domingo, R. Frey, Q. Ingram, H. Jantzen, G. Kyle, D. Renker and R.A. Schumacher, Nucl.Phys. **A469** (1987) 617.

[19]E. Bellotti, D. Cavalli and C. Matteuzzi, Nuovo Cimento **18A** (1973) 75.

[20]H. Yokota, T. Mori, T. Katsumi, S. Igarashi, K. Hama, R. Chiba, K. Nakai, J. Chiba, H. En'yo, S. Sasaki, T. Nagae and M. Sekimoto, Phys.Rev.Lett. **58** (1987) 191.

[21]Z. Papandreou, G.J. Lolos, G.M. Huber, J.C. Cormier, S.I.H. Naqvi, D.F. Ottewell, P.L. Walden and G. Jones, Phys.Lett.**227B** (1989) 25.

[22]G. Backenstoss, D. Brodbeck, M. Iżycki, P.Salvisberg, M.Steinacher, P. Weber, H.J. Weyer, A. Hoffart, B. Rzehorz, H. Ullrich, D. Bosnar, M. Furić and T. Petković, Phys.Rev.Lett. **61** (1988) 923.

[23]Z. Papandreou, G.J. Lolos, G.M. Huber and X. Aslanoglou, NIM **A268** (1988) 179.
Z. Papandreou, G.J. Lolos, G.M. Huber, J.C. Cormier, S.I.H. Naqvi, E.L. Mathie, D.F. Ottewell, P.L. Walden, G. Jones, R.P. Trelle, X. Aslanoglou and S. Orfanakos, NIM **B34** (1988) 454.

[24]G.R. Smith, D.R. Gill, D. Ottewell, G.D. Wait, P. Walden, R.R. Johnson, R. Olszewski, R. Rui, M.E. Sevior, R.P. Trelle, J. Brack, J.J. Kraushaar, R.A. Ristinen, H. Chase, E.L. Mathie, V. Pafilis, R.B. Schubank, N.R. Stevenson, A. Rinat and Y. Alexander, Phys.Rev. **C38** (1988) 240.

[25]J.M. McAlister, M.Sc. thesis, University of British Columbia, unpublished (1988).

[26]F. James; CERN Computer Centre Program Library, W515, (1975).

[27]J.F.J. van den Brand, H.P. Blok, R. Ent, E. Jans, G.J. Kramer, J.B.J.M. Lanen, L. Lapikas, E.N.M. Quint, G. van der Steenhoven and P.K.A. de Witt Huberts, Phys.Rev.Lett. **60** (1988) 2006.

[28]P. Weber, J. McAlister, R. Olszewski, A. Feltham, M. Hanna, D. Humphrey, R.R. Johnson, G.J. Lolos, Y. Mardor, S. May-Tal, D. Ottewell, Z. Papandreou, M. Pavan, C. Ponting, F.M. Rozon, M. Sevior, G. Sheffer, G.R. Smith, V. Sossi, R. Tacik and D.Vetterli, Phys.Lett. **B233** (1989) 281.

[29]J.P. Schiffer, Comm.Nucl.Part.Phys. **14** (85) 15.

[30]G. Backenstoss, M. Iżycki, R. Powers, P.Salvisberg, M.Steinacher, P. Weber, H.J. Weyer, A. Hoffart, B. Rzehorz, H. Ullrich, D. Bosnar, M. Furić and T. Petković, Phys.Lett. **B222** (1989) 7.

[31]L. Salcedo, E. Oset, D. Strottman and E. Hernandez, Phys.Lett. **B208** (1988) 339.

[32]Our ^{4}He(π^+,pp) data at conjugate angles; M. Steinacher, Ph.D. thesis, University of Basel, 1988 (unpublished), and M. Steinacher et al., to be published.

[33]D. Ashery, Phys.Rev. **C36** (1987) 460.

[34]E. Oset, Y. Futami and H. Toki, Nucl.Phys. **A448** (1986) 597.

[35]S. Barshay, preprint (1989).

[36]G.E. Brown, H. Toki, W. Weise and A. Wirzba, Phys.Lett. **118B** (82) 39.
B. Schwesinger, A. Wirzba and G.E. Brown, Phys.Lett. **132B** (1983) 269.

[37]M. Baumgartner, H.P. Gubler, G.R. Plattner, W.D. Ramsay, H.W. Roser, I. Sick, P. Zupranski, J.P. Egger and M. Thies, Nucl.Phys. **A399** (1983) 451.

[38]G. Backenstoss, M. Iżycki, P.Salvisberg, M.Steinacher, P. Weber, H.J. Weyer, S. Cierjacks, B. Rzehorz, H. Ullrich, M. Furić and T. Petković and N. Šimičević, Phys.Rev.Lett. **59** (1987) 767.

[39]J. Källne, J.E. Bolger, M.J. Devereaux and S.L. Verbeck, Phys.Rev. **C24** (1981) 1102.

[40]D. Ashery, I. Navon, G. Azuelos, H.K. Walter, H.J. Pfeiffer and F.W. Schlepütz, Phys.Rev. **C23** (1981) 2173.

FIGURE CAPTIONS

Fig. 1 Schematic drawing of the experimental setup. (The distance to TA and TB is not drawn to scale).

Fig. 2 Schematic drawing of the ^{4}He target.

Fig. 3 Proton energy spectrum of the π^+d $\rightarrow$ pp reaction in the 2N center of mass system for RA=43.7° at T_{π^+}=165 MeV.

Fig. 4 A time-of-flight spectrum obtained in TA (bar 4) from the π^+d $\rightarrow$ pp reaction at T_{π^+}=165 MeV.

Fig. 5 Two-dimensional ΔE - E plot of RA for ^{4}He(π^+, ppp)n events. The particle separation is done with a box cut around the protons.

Fig. 6 Two-dimensional E - TOF plot of TA for ^{4}He(π^+, ppp)n events. The particle separation is done with a box cut around the protons.

Fig. 7 The X-, Y-, and Z- distributions of the target vertices for ^{4}He(π^+, ppp)n events.

Fig. 8 Missing mass distribution ($\theta_{RA} = 40°$, $\theta_{RB} = 136°$, and $\theta_{TA} = -55°$). The distribution peaks around the neutron mass M_n.

Fig. 9 Angular distributions of protons detected in TA and TB with RA=40° for a) RB=106°, b) RB=121°, and c) RB=136°. The solid dots are taken with MLU=3, the open circles are data with MLU=2. The solid lines refer to 3N and 4N phase space calculations as described in the text.

Fig. 10 Momentum distribution of the undetected neutron compared to 3N and 4N phase space calculations.

Fig. 11 Proton energy spectra as measured in a) RA, b) RB, and c) TA compared to 3N and 4N phase space calculations. The dashed line in c) is identical with the 3N phase space calculation but the energy is scaled by 0.92 to match the measured distribution.

Fig. 12 Proton energy spectra measured in RA, RB, and TA for RA=40^0, TA=-70^0, and a) RB=136^0, b) RB=121^0, and c) RB=106^0 respectively. The solid and dashed lines refer to 3N and 4N phase space calculations respectively.

Fig. 13 Missing momentum distributions for different energy cuts imposed on T_p(TA) as described in the text.

Fig. 14 Energy plot T_p(TA) vs. T_p(RB) for a) ^{4}He(π^+, ppp)n data and b) 3N phase space MC events.

Fig. 15 Energy plot T_p(TA) vs. T_p(RA) for a) ^{4}He(π^+, ppp)n data and b) 3N phase space MC events.

Table 1. Compilation of measured counter configurations:

Configuration	θ_{RA} [deg]	θ_{RB} [deg]	θ_{TA} [deg]	θ_{TB} [deg]
I	40	106,121,136	-55	-126
II	40	106,121,136	-70	
III	40	106,121,136	-40	-100

Table 2. Compilation of measured counter configurations, Monte Carlo acceptance, event fraction due to 3N and 4N, and deduced cross sections (the numbers given in brackets have large uncertainties due to poorly determined contributions of $d\sigma^{3N}$ and $d\sigma^{4N}$) :

Conf.	θ_{RA} [deg]	θ_{RB} [deg]	θ_{TA} [deg]	θ_{TB} [deg]	G_A^{3N} [10^{-4}]	G_A^{4N} [10^{-4}]	$d\sigma^{3N}$ / $d\sigma^{4N}$ [%]	σ^{3N} [mb]	σ^{4N} [mb]
1	40	106	-40			0.10			1.8
2	40	106	-55		0.21	0.19	83/17	4.1	0.9
3	40	106	-70		1.06	0.28	92/ 8	4.4	1.4
4	40	121	-40		0.10	0.16	(38/62)	(3.4)	(3.4)
5	40	121	-55		0.73	0.27	88/12	4.9	1.8
6	40	121	-70		1.74	0.34	92/ 8	4.8	1.8
7	40	136	-40		0.48	0.27	(80/20)	(7.2)	(3.2)
8	40	136	-55		1.64	0.36	93/ 7	5.1	1.7
9	40	136	-70		1.90	0.39	92/ 8	5.3	2.4
10	40	106		-100	0.67	0.27	(53/47)	(2.2)	(4.8)
11	40	106		-126		0.10			1.7
12	40	121		-100	0.30	0.23	(44/56)	(2.7)	(4.4)
13	40	121		-126		0.06			2.9
14	40	136		-100	0.16	0.20	(33/67)	(2.8)	(4.4)
15	40	136		-126		0.04			1.7

Table 3. Compilation of absorption cross sections σ^{3N} and σ^{4N}:

Reaction	process	T_π [MeV]	cross section [mb]	reference
^{4}He(π^+,ppp)n	3N	165	4.8 ± 1.0	present data
^{4}He(π^+,ppp)n	4N	165	< 2.0	present data
^{4}He(π^+,ppp)n	3N	120	2.1 ± 0.5	[22]
^{4}He(π^+,ppn)p	3N	120	4.3 ± 0.8	[22]
^{4}He(π^+,ppp)n	4N	120	0.5 ± .15	[22]
^{3}He(π^+,pp)p	3N	120	3.9 ± 0.5	[14]
^{3}He(π^+,pp)p	3N	350	1.8 ± 0.16	[15]
^{3}He(π^+,pp)p	3N	500	0.64 ± 0.08	[15]
^{3}He(π^-,pn)n	3N	120	3.7 ± 0.6	[14]

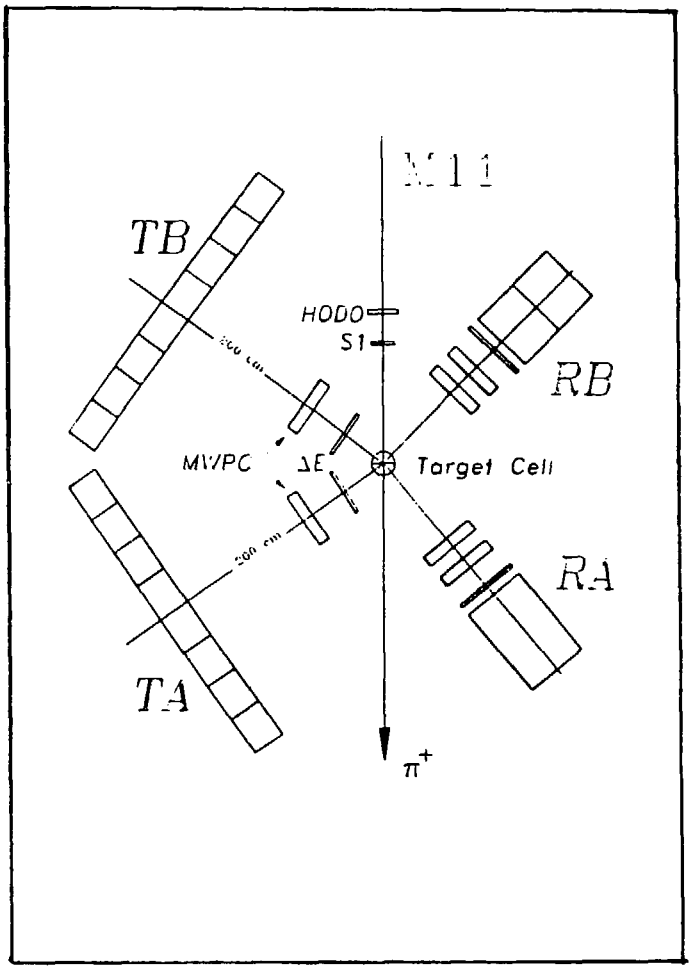
M11
TB
HODO
S1
RB
MWPC
ΔE
Target Cell
RA
TA
π+

Fig. 1

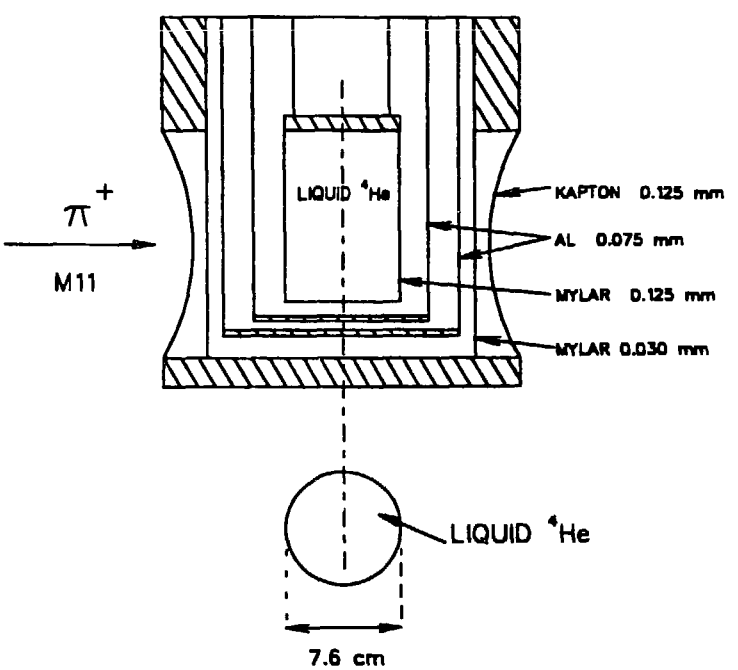
π+
M11
LIQUID ⁴He
KAPTON 0.125 mm
AL 0.075 mm
MYLAR 0.125 mm
MYLAR 0.030 mm
LIQUID ⁴He
7.6 cm

Fig. 2.

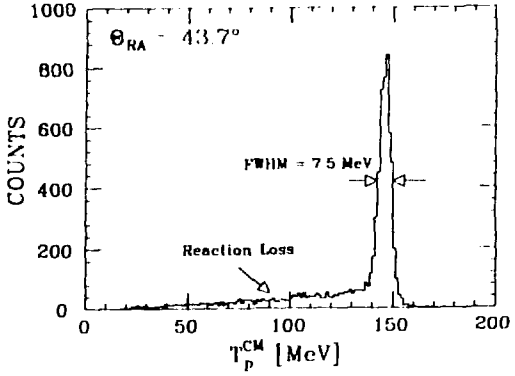

Fig. 3

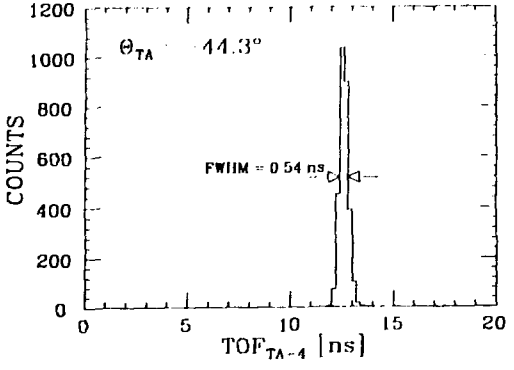

Fig. 4

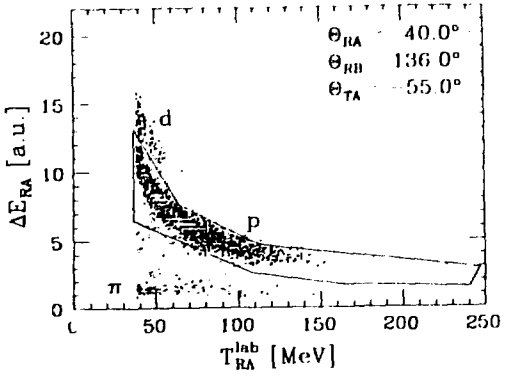

Fig. 5

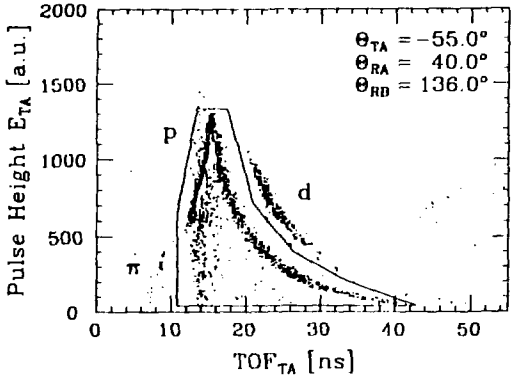

Fig. 6

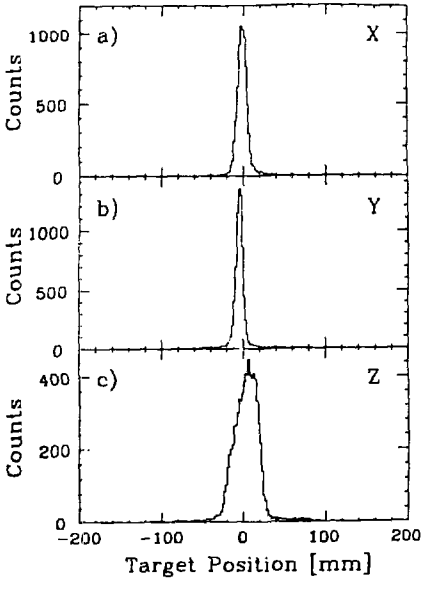

Fig. 7

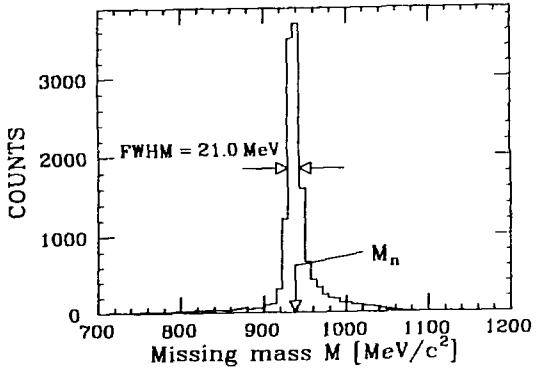

Fig. 8

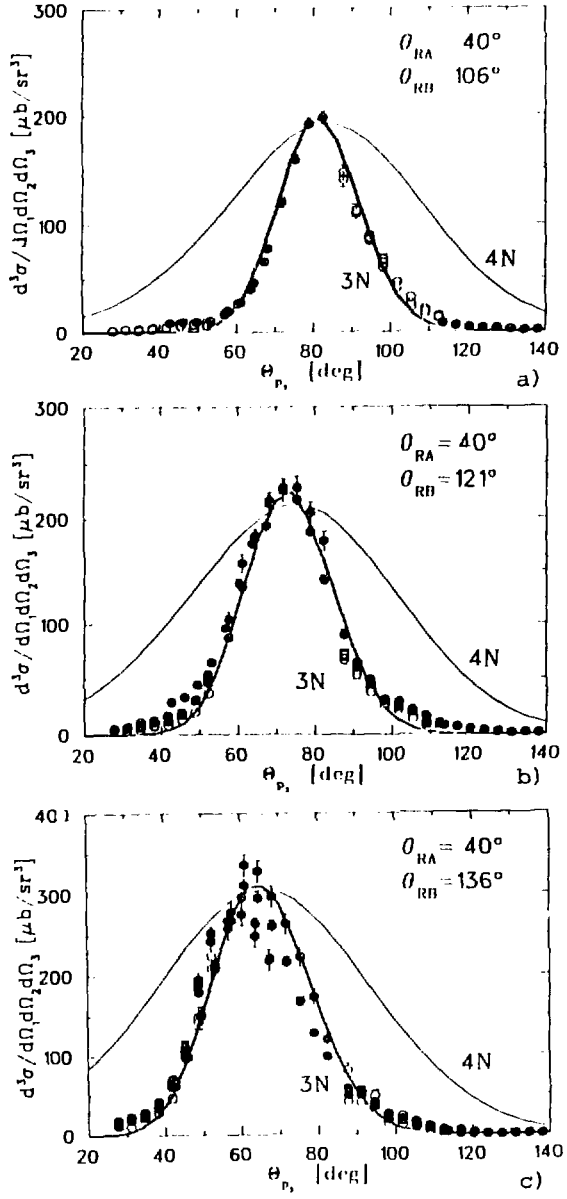

Fig. 9

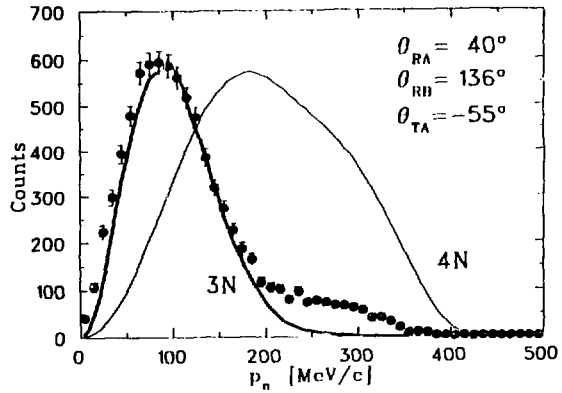

Fig. 10

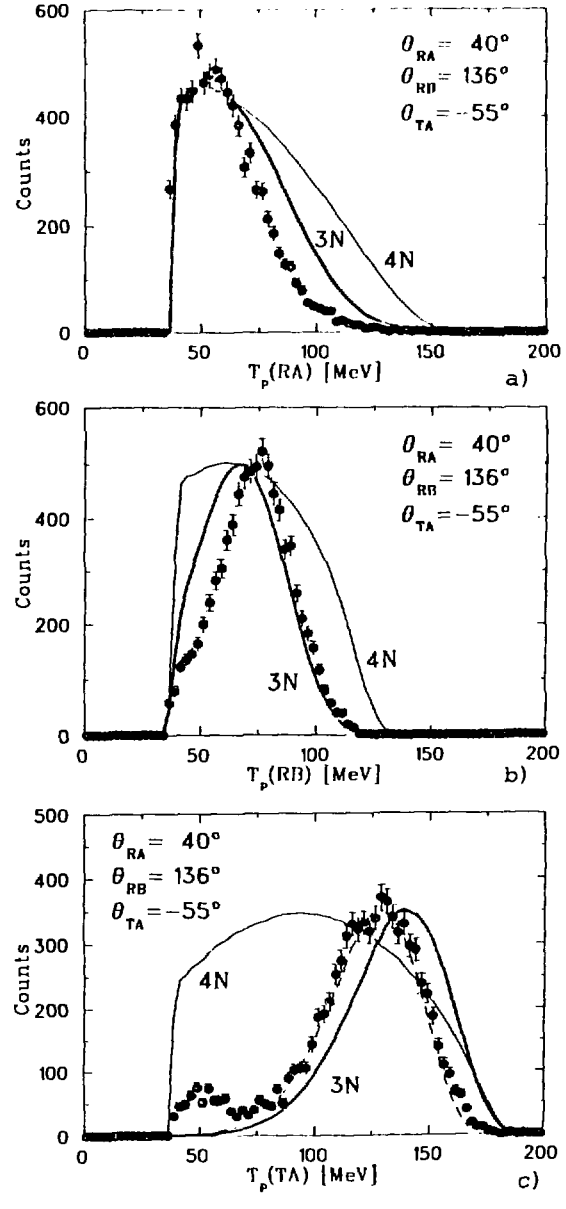

Fig. 11

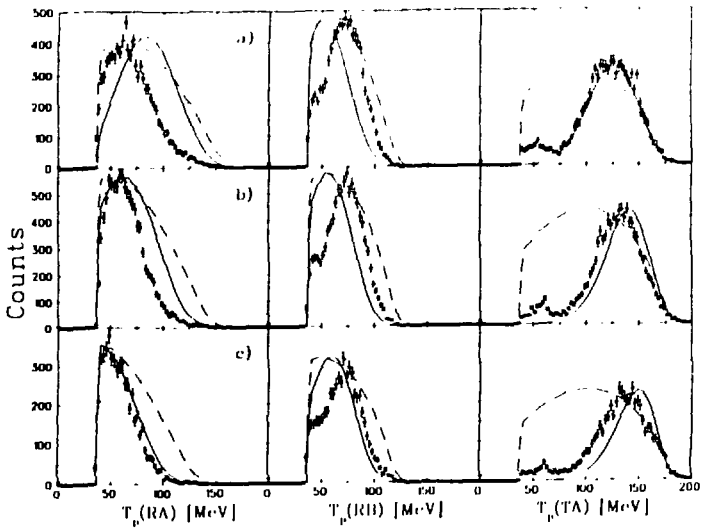

Fig. 12

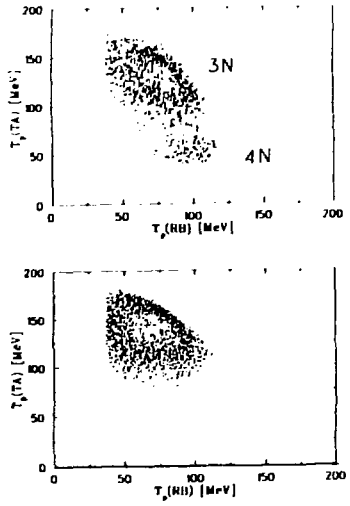

Fig. 14

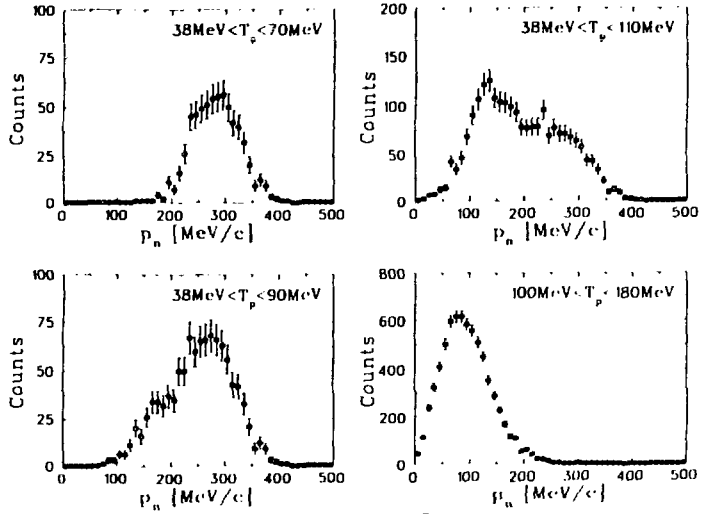

Fig. 13

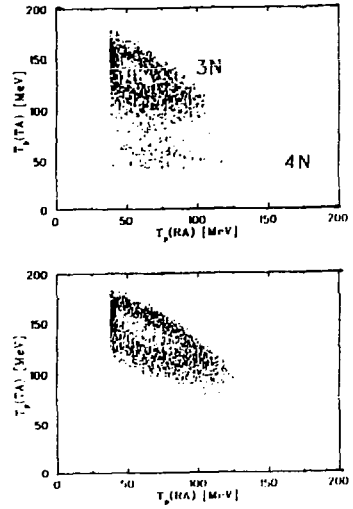

Fig. 15